Air-Steam Etched Construction of Hierarchically Porous Metal-Organic Frameworks

Author names

Hongliang Huang[#], Yuxiu Sun[#], Xuemeng Jia[#], Wenjuan Xue, Chenxu Geng, Xin Zhao, Donghai Mei[*], Chongli Zhong[*]*

Affiliations

State Key Laboratory of Membrane Separation and Membrane Processes, School of Chemistry and Chemical Engineering, Tiangong University, Tianjin 300387, P. R. China

Corresponding author

zhongchongli@tjpu.edu.cn (C.Z.);

dhmei@tiangong.edu.cn (D.M.);

yuxiusun@tiangong.edu.cn (Y.S.).

.

Abstract

The introduction of mesoporosity into the microporous metal-organic frameworks (MOFs) is expected to expand their applications. Herein, we report a green and facile method to obtain hierarchically porous MOF structures by using an air-steam etching process. By virtue of the protonation reaction between the imidazole moiety and water vapor, the protonated imidazole related linkers leave the framework, resulting in the formation of mesopores in the zeolitic imidazolate frameworks (ZIFs), as exemplified by ZIF-8. Given the mild etching process, the materials' structural integrity and crystallinity are well maintained. Remarkably, the proposed steam etching approach is generally applicable, which can be readily extended to other ZIFs, such as ZIF-14, ZIF-69, and ZIF-71, thus representing a powerful strategy to construct hierarchically porous MOF materials.

Keywords: hierarchical pores • metal-organic frameworks • steam etching • green engineering • reaction kinetics

Introduction

Chemical etching is a simple and accessible processing technology, widely used in areas of the semiconductor manufacturing process and pattern processing,[1] among which, wet etching has attracted much attention, given the advantages of good selectivity, well repeatability, and simple equipment.[2] Very recently, numerous efforts have been devoted to applying wet etching to tailoring the size, morphology, or porosity of advanced nanomaterials such as zeolites and metal-organic frameworks (MOFs).[3-6] However, a large number of harmful chemical reagents, such as strong acid and base, are often adopted in wet etching processes,[7] which cannot meet the requirements of sustainable development.[8] Therefore, the exploration of an environmentally friendly etching agent and a solvent-free etching process is highly desired.

Zeolitic imidazolate frameworks (ZIFs), a sub-class of MOFs based on divalent metal cations and imidazolate linkers in the analogous zeolite structure, are attractive for a wide range of applications.[9-12] Although ZIFs exhibit unique features including high surface area, excellent chemical/thermal stability, and exceptional synthetic tunability of the pore structure, most of them are microporous structures, which greatly hinders the mass transfer and prevents the access of large molecules, thus restricts their applications.[13,14] To address this challenge, attentions have been paid to prepare hierarchically porous MOFs (H-MOFs) with strategies mainly including: (a) pre-engineered linker with extensional length; [15-18] (b) diversified template-based approach; [19-26] (c) defect formation strategy; [27, 28] and others e.g. hydrolysis, ozonolysis, and thermolysis

method.[29-31] Although the ligand-extension strategy can create periodic nanostructures of MOFs, the complicated synthesis procedure of organic linkers and high cost limit their large scale production and real applications significantly. More importantly, the longer linkers normally result in the reduced stability of MOFs. In contrast, many stable H-MOFs can be prepared by a template-based approach or defect formation strategy. However, excess of templates or modulators are adopted in the H-MOF synthesis, and many organic solvents are involved during the post-treatment process. Even worse, the use of templates will inevitably reduce the crystallinity of the material. For the ozonolysis or thermolysis method, specific ozone- or thermo-sensitive structure units need to be predesigned in pristine MOFs, thus greatly reducing the generality of H-MOFs construction. To this end, developing green and sustainable approaches for the construction of H-MOFs featuring simply and feasibly manner is imperative, yet challenging to date.

With these considerations, we proposed a steam-etching strategy to prepare H-ZIFs in air by taking advantage of the controllable protonation reaction between the imidazole moiety and water vapor. In addition, given that only water vapor is involved in the etching process, the developed green approach is universal and scalable. More importantly, the degree of mesoporosity in the resulting H-ZIFs can be easily controlled by adjusting the etching conditions in terms of time and temperature.

Experiment

Steam etching treatment of MOFs in air. Taking ZIF-8 as a typical example, 0.100 g of ZIF-8 sample was dispersed in a quartz boat and put it to the muffle furnace. The temperature of the furnace was increased to target temperature at a rate of 5 ^{o}C/min, and maintained for a target time. After that, the temperature of the furnace was declined to room temperature at a rate of 5 ^{o}C/min.

Heating treatment of MOFs under dry or humid environment. For the comparative study, a series of heating treatment was performed in a tube furnace. Typically, 0.100 g of MOF sample was dispersed in a quartz boat and then placed to a tube furnace. The tube was connected with compressed air or nitrogen gas cylinder, between them a bubbling bottle containing 0.1 M NaOH aqueous solution and a desiccator set were located. Then, the furnace was heated to a target temperature at a rate of 5 ^{o}C/min under gas flow of 20-80 mL/min, and maintained for 60 min, which gave the heated MOF sample under dry condition.

Characterization. Powder X-ray diffraction (PXRD) data were collected on a Bruker D2 Phaser X-ray powder diffractometer equipped with graphite mono-chromatized Cu K radiation (λ = 1.54056 Å) at 30 kV and 10 mA. Nitrogen sorption isotherms were measured using a Micromeritics ASAP 2020 system at 77 K. The surface area is acquired using the Brunauer-Emmett-Teller (BET) method. The scanning electron microscopy (SEM) images were recorded on a Gemini SEM 500 instrument. The transmission electron microscopy (TEM) and energy dispersive X-ray (EDX) elemental mapping were collected using a TALOS F200X transmission electron microscope with an accelerating voltage of 20 kV. Thermogravimetry analysis (TGA)

was performed at a rate of 10 ºC/min under N_2 flow using a Netzsch STA 409 thermal analyzer. The combined TGA-MS analysis was performed in Hitachi TG/DTA 7300 with an attached LC-DC200M PRO Mass Spectrometer under air flow. Fourier transform infrared (FT-IR) measurement was carried out on a Bruker TENSOR II FT-IR spectrometer. UV-vis spectra were obtained using a UV-2600 spectrophotometer. The metal content of ZIF-8 was determined using an inductively coupled plasma Mass spectrometer (ICP-MS, PerkinElmer NexION 300D ICP mass spectrometer). Elemental Analysis (EA) was used to determine the contents of nitrogen and carbon elements using a CARLO ERBA 1106. The X-ray photoelectron spectroscopy (XPS) spectrum was recorded on a Thermofisher K-alpha spectrometer. ^{1}H NMR (Bruker 400 M) spectra was used to determine the structure of collected powders and calculate the yield of product in the CO_2 cycloaddition with epichlorohydrin.

DFT calculation

The periodic ZIF-8 structure model with the cubic unit cell lengths of 16.991×16.991×16.991 Å^3 that was obtained from the experimental XRD results was used in this work.[32] All geometrical optimizations and transition state calculations were carried out using the QUICKSTEP program within the CP2K code,[33] employing a mixed Gaussian and planewave basis sets. Core electrons were represented with norm-conserving Goedecker-Teter-Hutter pseudopotentials, [34-36] and the valence electron wavefunction was expanded in a double zeta basis set with polarization functions (DZVP-MOLOPT-SR-GTH) [37] along with an auxiliary plane wave basis set with an energy cutoff of 500 Ry. The generalized gradient approximation exchange-correlation functional

of Perdew, Burke, and Enzerhof (PBE) [38] was used. To account for the van der Waals (vdW) dispersion interaction, the DFT-D3 scheme with an empirical damped potential term was added into the energies obtained from exchange-correlation functional in the calculations. The BFGS algorithm with SCF convergence criteria of 1.0×10^{-8} au was used in geometrical optimizations. Test calculations showed that the energy change was negligible (<0.01 eV) when the maximum force convergence criteria of 0.001 hartree/bohr was used. Zero-point energy corrections were calculated on the basis of a normal-mode frequency analysis. The transition states were determined using the climbing image-nudged elastic band (CI-NEB) method.[39, 40] Seven intermediate images between initial and final states were used in transition state calculations.

Results and discussion

As a proof of concept, an initial steam etching process was performed by heating ZIF-8 at 350 ^{o}C for 60 min in an air atmosphere with a relative humidity of 50-60%. The schematic illustration of the steam etching process is shown in Scheme 1. After air steam etching, a distinct hysteresis loop appeared in the N_2 sorption isotherms of the treated ZIF-8, revealing the creation of mesopores, and the mesopore size distribution in H-ZIF-8 is centered at 3.9 nm (Figs. 1a and 1b). Furthermore, the generated hierarchical pores can also be corroborated by transmission electron microscopy (TEM) images (Figures 1c and 1d). The structural integrity of H-ZIF-8 is validated by the powder X-ray diffraction (PXRD) pattern, which is consistent with the pristine ZIF-8 in terms of relative intensity and position (Figures S1a and S1b). Moreover, this etching method offers a feasible and fast pathway for large-scale production of H-ZIF-8 powders in 60

min, demonstrated by straightforward scale-up from milligrams to 10 grams (Figure S2).

To test the controllability of this etching process, additional experiments were carried out. Given that temperature is a driving force for the reaction, we first compared the samples after being treated under various temperatures. At the temperature of 250 ^{o}C, the treated ZIF-8 maintained the original microporous character (Figure 2a). Increasing the temperature to 310 ^{o}C, a small hysteresis was observed for N_2 sorption isotherms of the treated ZIF-8, indicative of the occurrence of etching. The loop further increased along with the treating temperature increasing from 330 to 350 ^{o}C, suggestive of the increased mesoporosity in the resulting samples. The mesopore surface areas and the mesopore volumes of these treated H-ZIF-8 increased accordingly (Figure 2b and Table S1). Subsequently, the TEM observation clearly confirmed the generation of numerous irregular mesopores within H-ZIF-8 samples etched at different temperature (Figure 2c). However, further elevating temperature led to the disappearance of hysteresis loop in the adsorption isotherm and even complete collapse of ZIF-8 pore structure at 370 ^{o}C. Furthermore, the dwell time can also influence the creation of the hierarchical structure of ZIF-8. Figure S3a and Table S2 show the typical N_2 sorption isotherms and pore size distribution of the resultant ZIF-8 etched for different time in air at 350 ^{o}C. With the increase of dwell time, more and more obvious hysteresis loop appeared in the sorption curves firstly, followed by the obvious hysteresis loop disappeared, owing to the collapse of the ZIF-8 framework. In addition, Figure S3b demonstrates that the mesopore volume of H-ZIF-8 can also be tuned by etching time. The above results highlight controllable etching process and the adjustability of mesoporosity in H-ZIF-8 prepared by this air-steam etching approach.

To unveil the nature of creating hierarchical pores, the obtained H-ZIF-8 samples were characterized using various techniques. Firstly, although the PXRD patterns (Figure S4a) show that all the H-ZIF-8 samples etched from 310 to 350 ^{o}C for 60 min are in good match with the pristine ZIF-8, the peaks show a distinct shift to higher angles, implying a shrinking frame after etching treatment.[41] Next, the Fourier transform infrared spectroscopy (FT-IR) studies illustrate the retention of the original structure of ZIF-8 after etching (Figure S4b). In particular, intensity invariance of -CH_3 mode at 1384 cm^{-1}, C=N mode at 1584 cm^{-1}, CH bending of imidazolate structure at 1145 cm^{-1}, and Zn-N peak at 420-422 cm^{-1}, rules out the breakage mIm linker in etched ZIF-8 samples. [42-45] Besides, ^{1}H NMR spectra spectra (Figure S5) of all H-ZIF-8 are very similar to that of pristine ZIF-8, further indicating the retention of the original structure of imidazolate linker after etching treatment.

In addition, X-ray photoelectron spectroscopy (XPS) results show that a new broadening peak of C1s appeared as a shoulder at binding energy of 288.2 eV, and a negligible bump peak at around 292 eV (Figure S6a).[46] Meanwhile, the slight peak shift of the symmetric N 1s peak (Figure S6b) as well as the Zn 2p3/2 and Zn 2p1/2 signals (Figure S7) were also observed in the etched ZIF-8, Those results demonstrate the formation of defects after creating hierarchical pores in all H-ZIF-8 samples. Moreover, the elemental analysis (Table S3) shows that both N and C element contents decreased gradually with the extension of dwell time at 350 ^{o}C, while the Zn content exhibited a significant rising trend in all H-ZIF-8 samples. All these results support the fact that the generation of hierarchical pores in ZIF-8 is derived from the removal of mIm linker in ZIF-8 during the steam etching.

Considering the low boiling point of HmIm ligand, it is postulated that the entire mIm can be removed from the ZIF-8 framework during etching process. To testify this envision, a combined thermogravimetry and mass-spectrometry (TG-MS) measurement was performed in air to demonstrate the removal of linker from ZIF-8 during the air steam etching. In Figure 3a, the TGA curve begins to slightly decline as the temperature exceeds 300 ^{o}C. The synchronous MS signals display intense peaks of CO_2 and NO, respectively, once the temperatures higher than 370 ^{o}C. However, in the region of 310 to 350 ^{o}C, there are no MS signals related to CO_2, NO, and NO_2, which rules out the possibility of linker pyrolyzation in the air steam etching process. For more in-depth analysis, the TGA curve in the range of 0 to 60 min and the corresponding MS signals at a constant temperature of 350 ^{o}C are typically shown in Figure 3b. Holding at a temperature of 350 ^{o}C, no other signals were detected even for the trace amount of CO_2, NO, and NO_2, while the weight of the sample continued to drop, which indicated a complete linker removal process before the collapse of the ZIF-8 framework. Furthermore, we collected some amount of white powder at the end of the gas outlet after etching treatment, and the ^{1}H NMR, and FT-IR characterizations strongly confirm that the collected white powder is the pure HmIm ligand (Figures 3c and 3d), thus providing direct evidence that the linkers were removed as a whole instead of decomposing.

To highlight the crucial role of water molecules in etching process, a set of control experiments were performed in a tube furnace at 350 ^{o}C for 60 min, and the schematic representation is shown in Figure 3e, where sodium hydroxide solution was used to offer humid environment while ruling out the effect of acidic gases such as CO_2 in path 1 and 2. As expected,

no hysteresis loop was observed in the treated ZIF-8 after treating under dry N_2 (path 3) or dry air (path 2) environment (Figure 3f). On the contrary, the obvious hysteresis loop emerged in the isotherms, proving the presence of mesopores in the treated ZIF-8 after etching in humid air (path 1), which strongly sustains the irreplaceable role of water molecule during the etching process. Furthermore, H-ZIF-8 treated with different water content was obtained by adjusting the air flow rate from 20 to 80 mL/min. As shown in Figure 3f and Table S4, more defective mesoporous structures are formed with increasing water content in the etching process. However, excess water contents (with an air flow rate of 80 mL/min) led to the much lower BET surface area (394 m^2/g) and weak PXRD patterns (Figure 3g), indicating the severe collapse of ZIF-8 framework when exposed to overmuch water molecules.

To further understand the underlying steam etching mechanism and linker removal process, periodic density functional theory (DFT) calculations were carried out. First, DFT calculations show that the linker would not decompose into fragments or methane, ethane etc. since they are highly endothermic (Figure S8, and Table S5). The direct Zn-N bond–breaking leading to the first defect site in ZIF-8 is also highly energy demanding (+119.9 kJ/mol). Furthermore, to break another Zn-N bond on the other side is not possible since the complete removal of mIm as a whole from ZIF-8 needs the detached linker to be protonated.[47-49] Instead, in the presence of water molecules, our calculations, as shown in Figure 4, indicate that the linker removal occurs in three steps: 1) the first Zn-N bond-breaking by the substitution of a water molecule; 2) the second Zn-N bond-breaking step involves both another water molecule substitution and the decomposition of first substituted water molecule, resulting in a protonated mIm linker (HmIm)

inside the ZIF-8 pore, and 3) diffusion of HmIm out of ZIF-8. The DFT calculations also suggest that the increase of water content decreases the activation barrier of the rate-limiting step (step 2), agreeing well with the experimental observation.

To verify the generality of this method, other ZIF materials (Table S6), such as ZIF-14, ZIF-71, and ZIF-69, were used to fabricate hierarchical ones. Guided by the TGA results of these chosen MOFs (Figure S9), appropriate etching temperature was determined carefully to avoid the collapse of the framework during steam etching. As expected, the mesopores arose after the steam etching treatment as indicated by N_2 sorption isotherms (Figure S10). In addition, the TEM images (Figure S11) further confirm the appearance of mesopores in the etched ZIF samples.

To examine the accessibility of mesopores emerged in the H-ZIF-8, dye molecule uptake experiments in both pristine ZIF-8 and H-ZIF-8 were carried out, and direct green 26 (DG 26) with large molecular size (18×35.1 Å) was selected as model molecule. Clearly, the H-ZIF-8 could efficiently adsorb dye molecules due to existence of rich hierarchical pores and the color of the H-ZIF-8 changed from light yellow to dark green (Figure S12). In addition, the difference of DG 26 uptake process for ZIF-8 and H-ZIF-8 was also identified by UV-vis spectra analysis (Figure S13), where the H-ZIF-8 adsorbs DG 26 molecule more efficiency than that of pristine ZIF-8, and the removal efficiency of DG 26 reaches over 99 % after equilibrium. Meanwhile, the CO_2 cycloaddition reaction with epichlorohydrin was also performed to verify the superiority of mesopores and defective site in etched ZIF-8 (Figure 5a). As expected, the yield of the epichlorohydrin to chloropropene carbonate reached 99 % for H-ZIF-8 at 60 h while the yield of

ZIF-8 is only 47 %. The experimental data were fitted by the pseudo-first-order kinetic model ($\ln(C_0/C)=kt$), as presented in Figure 5b and Table S7. The obtained reaction rate constant of H-ZIF-8 is 0.07667 h^{-1} which is about 6 times larger than that of pristine ZIF-8. The above results suggest that the H-ZIF-8 exhibited much better catalytic activity in the cycloaddition reaction when compared with ZIF-8, which could be attributed to the enlarged pore size, fast diffusion rate, as well as the accessible active sites. Besides, H-ZIF-8 exhibits good cycle stability (Figure S14a) and the subsequent PXRD pattern further confirmed the good structural stability of H-ZIF-8 after catalytic cycles (Figure S14b).

Conclusions

In summary, we proposed a green and facile air-steam etching approach to construct H-MOFs without using any templates or solvents. The degree of mesoporosity in H-ZIF-8 can be controlled by regulating the etching temperature and time, and the resulting hierarchical framework maintained the original integrated structure and excellent stability. The combinational study of control experiments and DFT calculations highlight the crucial role of water molecules in the etching process, and the removed linker molecules were observed directly. The method was successfully applied to ZIF-14, ZIF-69, and ZIF-71, illustrating the generality of the strategy. From the above analysis, we have reason to believe that this work will provide a facile and green way for designing and constructing multifunctional MOF materials with hierarchical pores for various applications.

Literature Cited

1. Franssila S. *Introduction to microfabrication*, Wiely, Chichester; 2010.

2. Pal P, Sato K. A comprehensive review on convex and concave corners in silicon bulk micromachining based on anisotropic wet chemical etching. *Micro Nano Syst. Lett.* 2015; 3: 6-44.

3. Hu M, Ju Y, Liang K, Suma T, Cui J, Caruso F. Void engineering in metal-organic frameworks *via* synergistic etching and surface functionalization. *Adv. Funct. Mater.* 2016; 26: 5827-5834.

4. Avci C, Ariñez-Soriano J, Carné-Sánchez A, *et al.* Post-synthetic anisotropic wet-chemical etching of colloidal sodalite ZIF crystals. *Angew. Chem. Int. Ed.* 2015; 54: 14417-14421.

5. Koo J, Hwang I C, Yu X, Saha S, Kim Y, Kim K. Hollowing out MOFs: hierarchical micro- and mesoporous MOFs with tailorable porosity *via* selective acid etching. *Chem. Sci.* 2017; 8: 6799-6803.

6. Chang G G, Ma X C, Zhang Y X, *et al*. Construction of hierarchical metal-organic frameworks by competitive coordination strategy for highly efficient CO_2 conversion. *Adv. Mater.* 2019; 31: 1904969-1904977.

7. Hatsuki R, Yamamoto T. Nanoscale etching and flattening of metals with ozone water. *Nano*

Lett. 2012; 12: 3158-3161.

8. Mauter M S, Zucker I, Perreault F, Werber, J.R.,Kim J.H, Elimelech, M. The role of nanotechnology in tackling global water challenges. *Nature Sustainability.* 2012; 1: 166-175.

9. Li J R, Kuppler R J, Zhou H C. Selective gas adsorption and separation in metal-organic frameworks. *Chem. Soc. Rev.* 2009; 38: 1477-1504.

10. Dhakshinamoorthy, A, Li Z, Garcia H. Catalysis and photocatalysis by metal organic frameworks. *Chem. Soc. Rev.* 2018; 47: 8134-8172.

11. Chen B L, Yang Z X, Zhu Y Q, Xia Y D. Zeolitic imidazolate framework materials: recent progress in synthesis and applications. *J. Mater. Chem. A* 2014; 2: 16811-16831.

12. Li P. *et al.* Metal-organic frameworks with photocatalytic bactericidal activity for integrated air cleaning. *Nat. Commun*. 2019; 10: 2177.

13. Howarth A J, Liu Y, Li P, *et al.* Chemical, thermal and mechanical stabilities of metal-organic frameworks. *Nat. Rev. Mater.* 2016; 1: 15018.

14. Yuan S, Zou L, Qin J S, *et al.* Construction of hierarchically porous metal-organic frameworks through linker labilization. *Nat. Commun.* 2017; 8: 15356.

15. Yang J, Zhang, Y B, Liu Q, *et al.* Principles of designing extra-large pore openings and cages in zeolitic imidazolate frameworks. *J. Am. Chem. Soc.* 2017; 139: 6448-6455.

16. Park J, Wang Z U, Sun L B, Chen Y P, Zhou H C. Introduction of functionalized mesopores to metal-organic frameworks via metal-ligand-fragment coassembly. *J. Am. Chem. Soc.* 2012; 134: 20110-20116.

17. Feng D, Gu Z Y, Li J R, Jiang H L, Wei Z, Zhou H C. Zirconium-metalloporphyrin PCN-222: mesoporous metal-organic frameworks with ultrahigh stability as biomimetic catalysts. *Angew. Chem. Int. Ed.* 2012; 51: 10307-10310.

18. Feng L, Yuan S, Li J L, *et al.* Uncovering two principles of multivariate hierarchical metal-organic framework synthesis via retrosynthetic design. *ACS Cent. Sci.* 2018; 4: 1719-1726.

19. Cao S, Gody G, Zhao W, *et al.* Hierarchical bicontinuous porosity in metal-organic frameworks template from functional block co-oligomer micelles. *Chem. Sci.* 2013; 4: 3573-3577.

20. Junggeburth S C, Schwinghammer K, Virdi K S, Scheu C, Lotsch B V. Towards mesostructured zinc imidazolate frameworks. *Chem. Eur. J.* 2012; 18: 2143-2152.

21. Huang H, Li J R, Wang K, *et al.* An *in situ* self-assembly template strategy for the preparation of hierarchical-pore metal-organic frameworks. *Nat. Commun.* 2015; 6: 8847.

22. Wu Y, Zhou M, Zhang B, *et al.* Amino acid assisted templating synthesis of hierarchical zeolitic imidazolate framework-8 for efficient arsenate removal. *Nanoscale* 2014; 6: 1105-1112.

23. Shen K, Zhang L, Chen X, *et al.* Ordered macro-microporous metal-organic framework

single crystals. *Science* 2018; 359: 206-210.

24. Zhang F, Wei Y, Wu X, Jiang H, Wang W, Li H. Hollow zeolitic imidazolate framework nanospheres as highly efficient cooperative catalysts for [3+3] cycloaddition reactions. *J. Am. Chem. Soc.* 2014;136: 13963-13966.

25. Sun L B, Li J R, Park J, Zhou H C. Cooperative template-directed assembly of mesoporous metal-organic frameworks. *J. Am. Chem. Soc.* 2012; 134: 126-129.

26. Feng L, Li J L, Day G S, Lv X L, Zhou H C. Temperature-controlled evolution of nanoporous MOF crystallites into hierarchically porous superstructures. *Chem* 2019; 5: 1265-1274.

27. Fang Z, Durholt J P, Kauer M, *et al.* Structural complexity in metal-organic frameworks: simultaneous modification of open metal sites and hierarchical porosity by systematic doping with defective linkers. *J. Am. Chem. Soc.* 2014; 136: 9627-9636.

28. Cai G, Jiang H L. A modulator-induced defect-formation strategy to hierarchically porous metal-organic frameworks with high stability. *Angew. Chem. Int. Ed.* 2017; 56: 563-567.

29. Kim Y, Yang T, Yun G, *et al.* Hydrolytic transformation of microporous metal-organic frameworks to hierarchical micro- and mesoporous MOFs. *Angew. Chem. Int. Ed.*, 2015; 54: 13273-13278.

30. Guillerm V, Xu H, Albalad J, Imaz I, Maspoch D. Postsynthetic selective ligand cleavage by solid-gas phase ozonolysis fuses micropores into mesopores in metal-organic frameworks.

*J. Am. Chem. Soc.*2018; 140, 15022-15030.

31. Feng L, Yuan S, Zhang L L, *et al.* Creating hierarchical pores by controlled linker thermolysis in multivariate metal-organic frameworks. *J. Am. Chem. Soc.* 2018; 140: 2363-2372.

32. Park K S, Ni Z, Côté A P, *et al.* Exceptional chemical and thermal stability of zeolitic imidazolate frameworks. *PNAS* 2006; 103: 10186-10191.

33. VandeVondele J, Krack M, Mohamed F, Parrinello M, Chassaing T, Hutter J. QUICKSTEP: Fast and accurate density functional calculations using a mixed Gaussian and plane waves approach. *Comput. Phys. Commun.* 2005; 167: 103-128.

34. Goedecker S, Teter M, Hutter J. Separable dual-space Gaussian pseudopotentials. *Phys. Rev. B* 1996; 54: 1703-1710.

35. Hartwigsen C, Goedecker S, Hutter J. Relativistic separable dual-space Gaussian pseudopotentials from H to Rn. *Phys. Rev. B* 1998; 58: 3641-3662.

36. Krack M, Parrinello M. All-electron ab-initio molecular dynamics. *Phys. Chem. Chem. Phys.* 2000; 2: 2105-2112.

37. VandeVondele J, Hutter J. Gaussian basis sets for accurate calculations on molecular systems in gas and condensed phases. *J. Chem. Phys.* 2007; 127: 114105.

38. Perdew J P, Burke K, Ernzerhof M. Generalized gradient approximation made simple. *Phys.*

Rev. Lett. 1996; 77: 3865.

39. Henkelman G, Jonsson H. A dimer method for finding saddle points on high dimensional potential surfaces using only first derivatives. *J. Chem. Phys.* 1999; 111: 7010-7022.

40. Henkelman G, Uberuaga B P, Jonsson H. A climbing image nudged elastic band method for finding saddle points and minimum energy paths. *J. Chem. Phys.* 2000; 113: 9901-9904.

41. Babu D J, He G, Hao J, *et al.* Restricting lattice flexibility in polycrystalline metal-organic framework membranes for carbon capture. *Adv. Mater.* 2019; 31: 1900855-1900860.

42. Kumari G, Jayaramulu K, Maji T K, Narayana C. Temperature induced structural transformations and gas adsorption in the zeilitic imidazolate framework ZIF-8: A Raman study. *J. Phys. Chem. A* 2013; 117: 11006-11012.

43. Gadipelli S, Travis W, Zhou W, Guo Z. A thermally derived and optimized structure from ZIF-8 with giant enhancement in CO_2 uptake. *Energy Environ. Sci.* 2014; 7: 2232-2238.

44. Hamid M R A, Park S, Kim J S, Lee Y M, Jeong H K. Synthesis of ultrathin zeolitic imidazolate framework ZIF-8 membranes on polymer hollow fibers using a polymer modification strategy for propylene/propane separation. *Ind. Eng. Chem. Res.* 2019; 58: 14947-14953.

45. Rapurello R L, Lozano L A, Ramos-Fernández, E V, Fernández J L, Zamaro J M. Post-synthetic modification of ZIF-8 crystals and films through UV light photoirradiation: Impact on the physicochemical behavior of the MOF. *ChemPhysChem* 2019; 20: 1-10.

46. Ganguly A, Sharma S, Papakonstantinou P, Hamilton J. Probing the thermal deoxygenation of graphene oxide using high-resolution in situ X-ray-based spectroscopies. *J. Phys. Chem. C* 2011; 115: 17009-17019.

47. Han C, Zhang C Y, Tyminska N, Schmidt J R, Sholl D S. Insights into the stability of zeolitic imidazolate frameworks in humid acidic environments from first-principles calculations. *J. Phys. Chem. C* 2018; 122: 4339-4348.

48. Han R, Sholl D S. Computational model and characterization of stacking faults in ZIF-8 polymorphs. *J. Phys. Chem. C* 2016; 120: 27380-27388.

49. Han R, Tyminska N, Schmidt J R, Sholl D S. Propagation of degradation-induced defects in zeolitic imidazolate frameworks. *J. Phys. Chem. C* 2019; 123: 6655-6666.

Acknowldgements

This work was supported by National Key Projects for Fundamental Research and Development of China (No. 2016YFB0600901), the Natural Science Foundation of China (Nos. 21536001, 21878229 and 21978212), and the Science and Technology Plans of Tianjin (Nos. 18PTSYJC00180 and 19PTSYJC00020).

Conflict of interest

The authors declare no conflict of interest

List of Figure Captions

Scheme 1 Schematic illustration of underlying principle of air-steam etching process for generating hierarchically porous structure in H-ZIF-8.

Figure 1 Nitrogen sorption isotherms of (a) pristine ZIF-8 and (b) H-ZIF-8; TEM images of (c) pristine ZIF-8 and (d) H-ZIF-8. Scale bar is 100 nm in (c), and (d).

Figure 2 (a) Nitrogen sorption isotherms of ZIF-8 samples after air-steam etching with different temperatures for 60 min; (b) the according mesopore volume of H-ZIF-8 samples; (c) TEM images of H-ZIF-8 obtained at different etching temperature. Scale bar is 100 nm.

Figure 3 TG curve and MS signals of ZIF-8 during the etching treatment (a) at temperature up to 400 ^{o}C with a heating rate of 5 ^{o}C /min, and (b) at fixed temperature of 350 ^{o}C for 60 min. Colour scheme of MS signals: black, CO_2 (m/z=44), red, NO (m/z=30), blue, NO_2 (m/z=46; (c) ^{1}H NMR spectra and (d) FT-IR spectra of the collected white powder; (e) Schematic illustration of simulated heating system under dry or humid environment; (f) Nitrogen sorption isotherms of ZIF-8 etched at 350 ^{o}C for 60 min under different conditions including dry or humid environment with different gas flow rate ranging from 20 to 80 mL/min; (g) PXRD patterns of ZIF-8 etched in humid environment with different air flow rate from 20 to 80 mL/min.

Figure 4 Formation mechanism of water molecules induced hierarchically porous structure created in ZIF-8 via complete linker removal. The black line and red line represent the relevant reaction path with the assistance of two water molecules and four water molecules, respectively.

Figure 5 (a) Catalytic performance of ZIF-8 and H-ZIF-8 samples in CO_2 cycloaddition with

epichlorohydrin. Reaction condition: catalyst 80 mg, temperature 85 °C, 1 atm CO_2 pressure. The yield is determined by ^{1}H NMR. (b) Kinetic curves of pseudo-first-order model for ZIF-8 and H-ZIF-8 samples in CO_2 cycloaddition with epichlorohydrin.

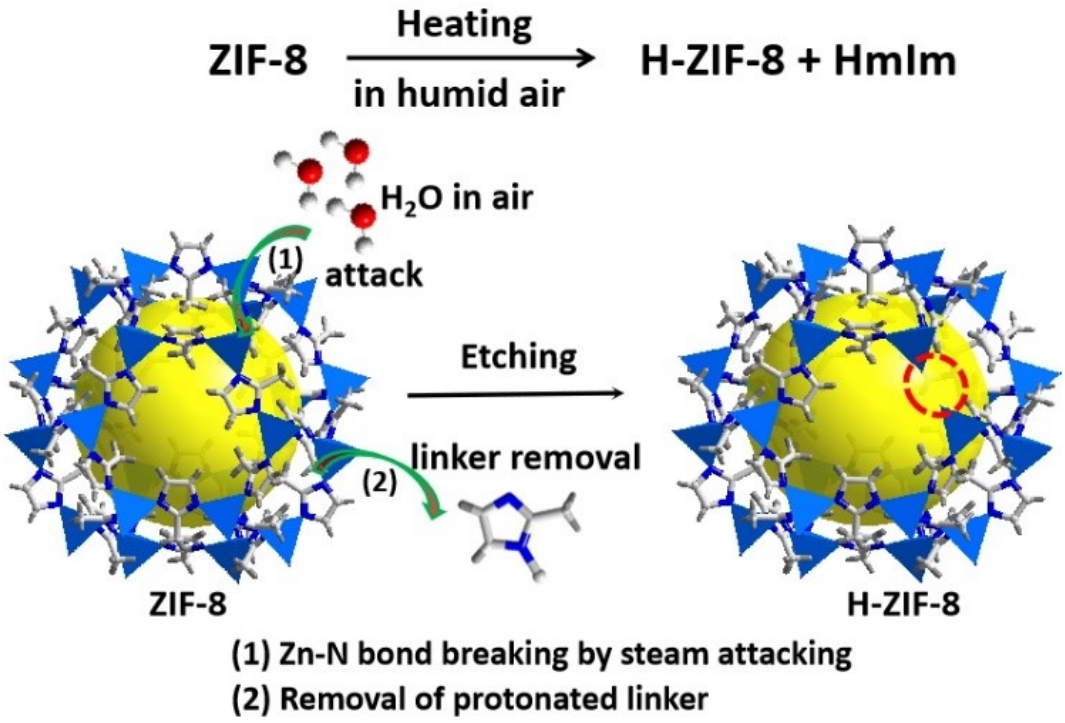

Scheme 1 Schematic illustration of underlying principle of air-steam etching process for generating hierarchically porous structure in H-ZIF-8.

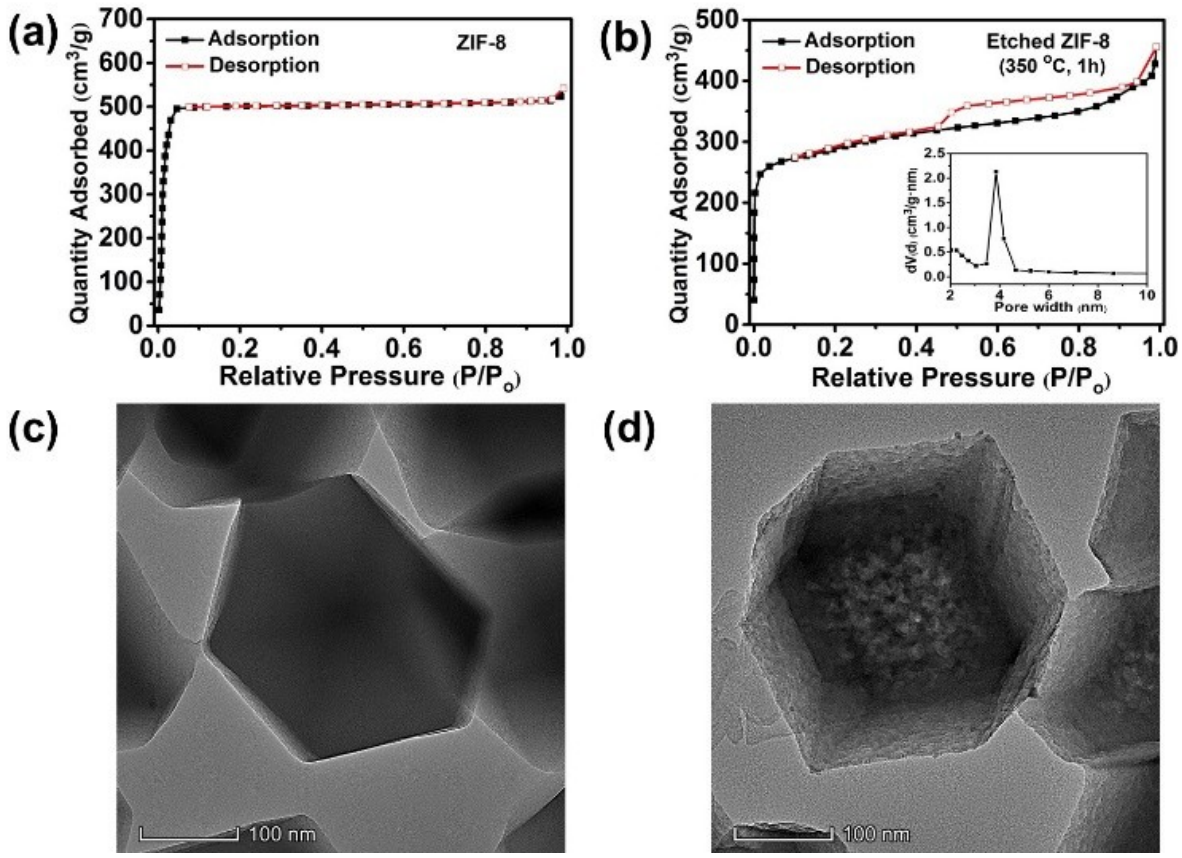

Figure 1 Nitrogen sorption isotherms of (a) pristine ZIF-8 and (b) H-ZIF-8; TEM images of (c) pristine ZIF-8 and (d) H-ZIF-8. Scale bar is 100 nm in (c), and (d).

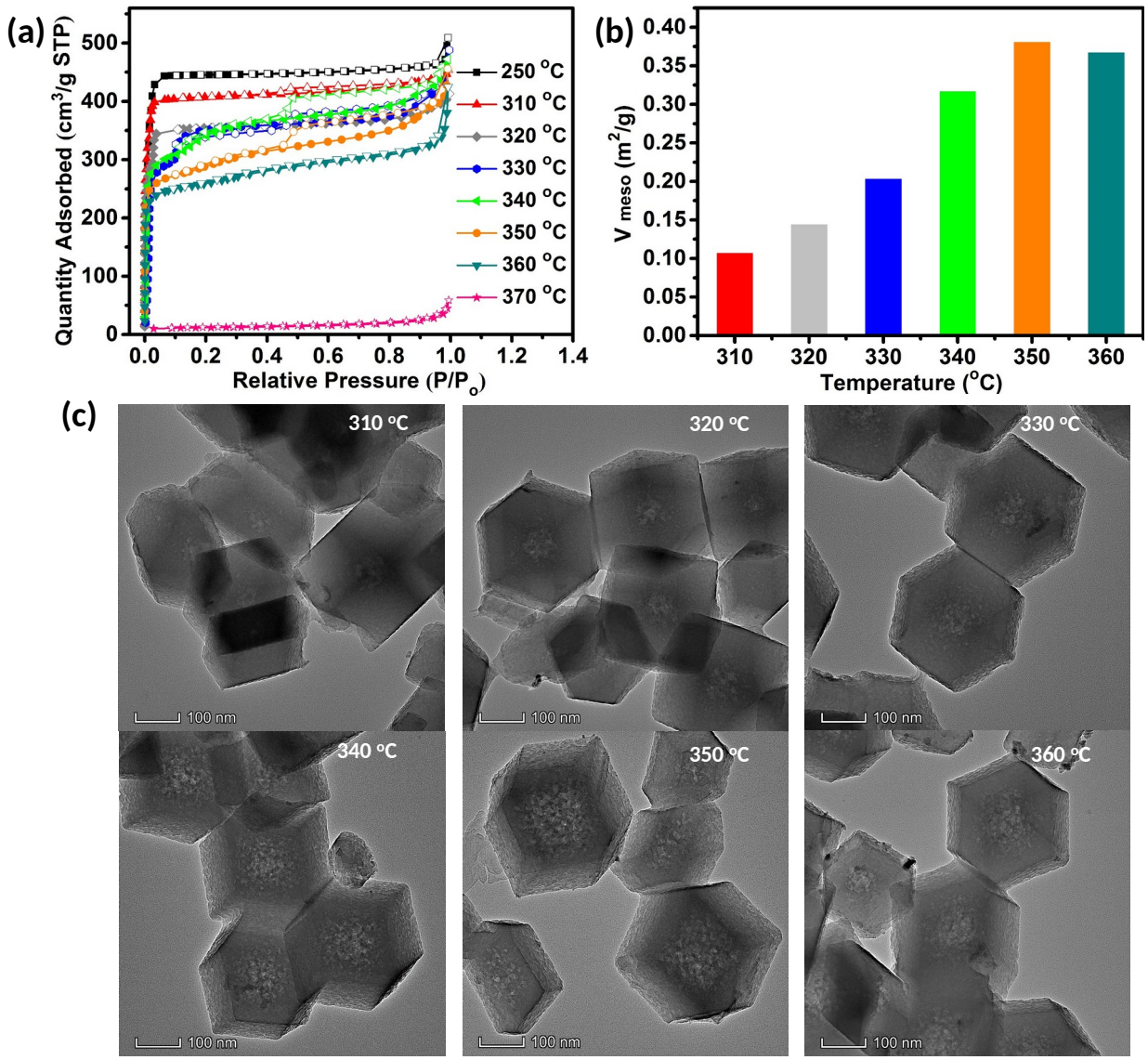

Figure 2 (a) Nitrogen sorption isotherms of ZIF-8 samples after air-steam etching with different temperatures for 60 min; (b) the according mesopore volume of H-ZIF-8 samples; (c) TEM images of H-ZIF-8 obtained at different etching temperature. Scale bar is 100 nm.

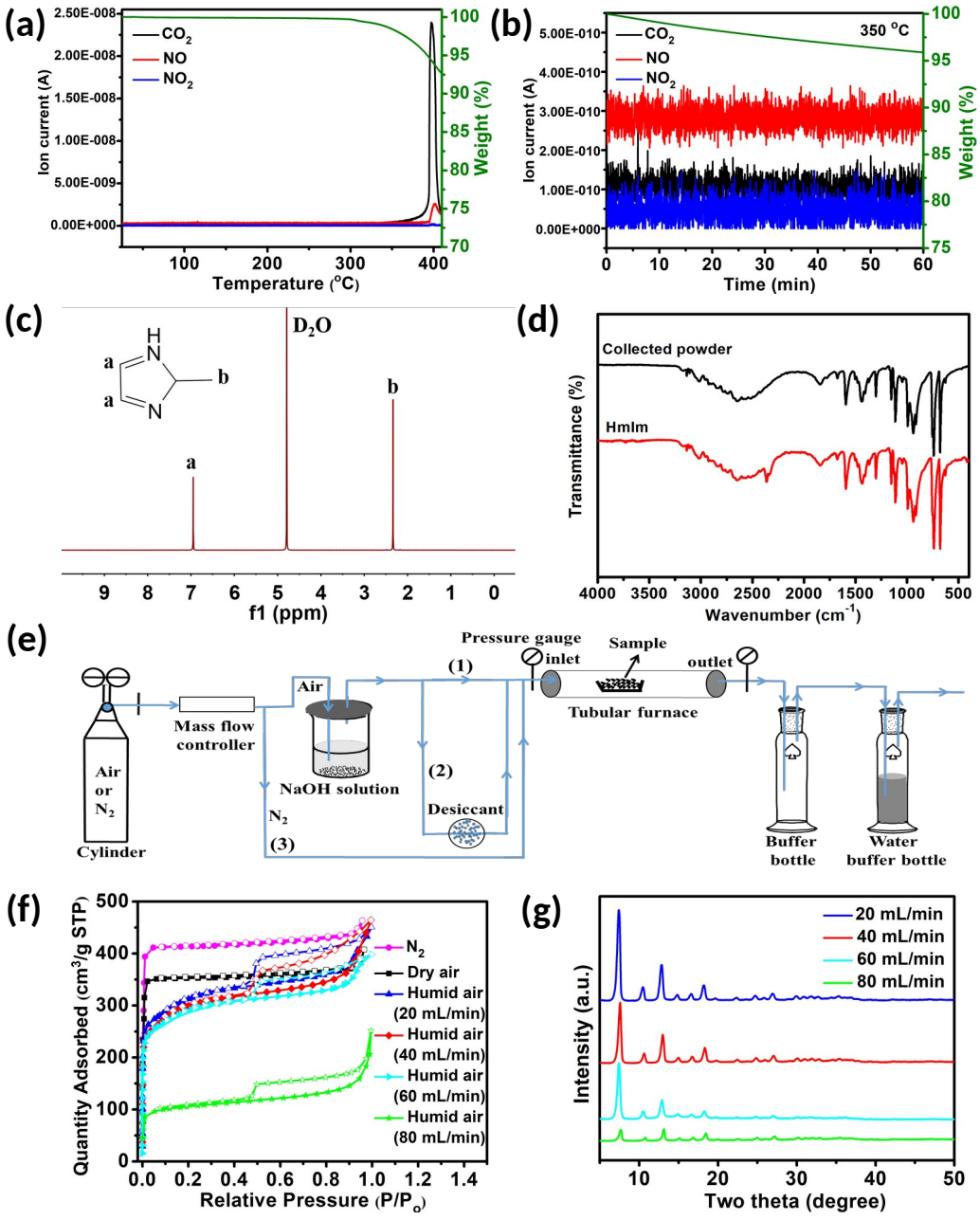

Figure 3 TG curve and MS signals of ZIF-8 during the etching treatment (a) at temperature up to 400 °C with a heating rate of 5 °C /min, and (b) at fixed temperature of 350 °C for 60 min. Colour scheme of MS signals: black, CO_2 (m/z=44), red, NO (m/z=30), blue, NO_2 (m/z=46; (c) ^{1}H NMR spectra and (d) FT-IR spectra of the collected white powder; (e) Schematic illustration of simulated heating system under dry or humid environment; (f) Nitrogen sorption isotherms of

ZIF-8 etched at 350 °C for 60 min under different conditions including dry or humid environment with different gas flow rate ranging from 20 to 80 mL/min; (g) PXRD patterns of ZIF-8 etched in humid environment with different air flow rate from 20 to 80 mL/min.

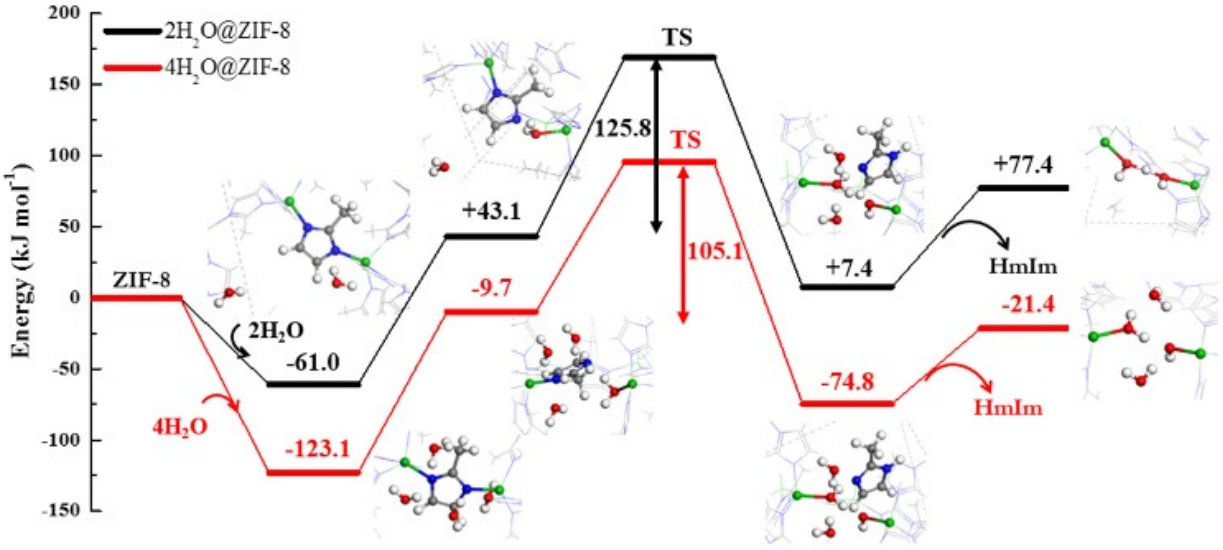

Figure 4 Formation mechanism of water molecules induced hierarchically porous structure created in ZIF-8 via complete linker removal. The black line and red line represent the relevant reaction path with the assistance of two water molecules and four water molecules, respectively.

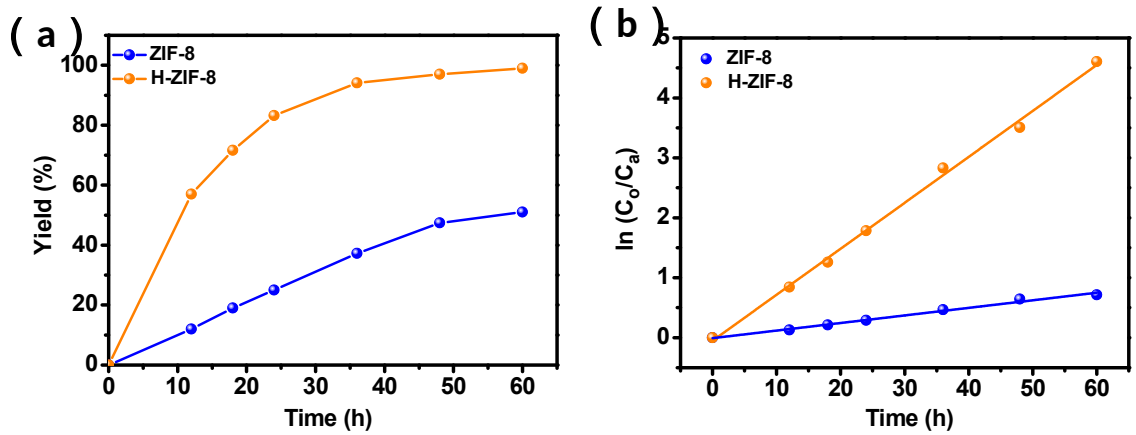

Figure 5 (a) Catalytic performance of ZIF-8 and H-ZIF-8 samples in CO_2 cycloaddition with epichlorohydrin. Reaction condition: catalyst 80 mg, temperature 85 °C, 1 atm CO_2 pressure. The yield is determined by ^{1}H NMR. (b) Kinetic curves of pseudo-first-order model for ZIF-8 and H-ZIF-8 samples in CO_2 cycloaddition with epichlorohydrin.